

Cite this: *Nanoscale*, 2015, **7**, 5249

# Core–shell hybrid upconversion nanoparticles carrying stable nitroxide radicals as potential multifunctional nanoprobes for upconversion luminescence and magnetic resonance dual-modality imaging†

Chuan Chen,<sup>a</sup> Ning Kang,<sup>b</sup> Ting Xu,<sup>a</sup> Dong Wang,<sup>a,b</sup> Lei Ren<sup>\*b</sup> and Xiangqun Guo<sup>\*a</sup>

Nitroxide radicals, such as 2,2,6,6-tetramethylpiperidine 1-oxyl (TEMPO) and its derivatives, have recently been used as contrast agents for magnetic resonance imaging (MRI) and electron paramagnetic resonance imaging (EPRI). However, their rapid one-electron bioreduction to diamagnetic *N*-hydroxy species when administered intravenously has limited their use in *in vivo* applications. In this article, a new approach of silica coating for carrying stable radicals was proposed. A 4-carboxyl-TEMPO nitroxide radical was covalently linked with 3-aminopropyl-trimethoxysilane to produce a silanizing TEMPO radical. Utilizing a facile reaction based on the copolymerization of silanizing TEMPO radicals with tetraethyl orthosilicate in reverse microemulsion, a TEMPO radicals doped SiO<sub>2</sub> nanostructure was synthesized and coated on the surface of NaYF<sub>4</sub>:Yb,Er/NaYF<sub>4</sub> upconversion nanoparticles (UCNPs) to generate a novel multifunctional nanoprobe, PEGylated UCNPs@TEMPO@SiO<sub>2</sub> for upconversion luminescence (UCL) and magnetic resonance dual-modality imaging. The electron spin resonance (ESR) signals generated by the TEMPO@SiO<sub>2</sub> show an enhanced reduction resistance property for a period of time of up to 1 h, even in the presence of 5 mM ascorbic acid. The longitudinal relaxivity of PEGylated UCNPs@TEMPO@SiO<sub>2</sub> nanocomposites is about 10 times stronger than that for free TEMPO radicals. The core–shell NaYF<sub>4</sub>:Yb,Er/NaYF<sub>4</sub> UCNPs synthesized by this modified user-friendly one-pot solvothermal strategy show a significant enhancement of UCL emission of up to 60 times more than the core NaYF<sub>4</sub>:Yb,Er. Furthermore, the PEGylated UCNPs@TEMPO@SiO<sub>2</sub> nanocomposites were further used as multifunctional nanoprobes to explore their performance in the UCL imaging of living cells and *T*<sub>1</sub>-weighted MRI *in vitro* and *in vivo*.

Received 24th December 2014,  
Accepted 9th February 2015

DOI: 10.1039/c4nr07591a  
[www.rsc.org/nanoscale](http://www.rsc.org/nanoscale)

<sup>a</sup>The MOE Key Laboratory of Spectrochemical Analysis and Instrumentation, State Key Laboratory of Physical Chemistry of Solid Surfaces, Department of Chemistry, College of Chemistry and Chemical Engineering, Xiamen University, Xiamen 361005, P. R. China. E-mail: xqguo@xmu.edu.cn, renlei@xmu.edu.cn;  
Fax: +86 0592 2181682; Tel: +86 0592 2181682

<sup>b</sup>Department of Biomaterials, College of Materials, Xiamen University, Xiamen 361005, P. R. China

† Electronic supplementary information (ESI) available: ESI-MS spectrum, TEM image and ESR spectra of the silanizing nitroxide radical precursor and TEMPO@SiO<sub>2</sub> nanoparticles. Schematic illustration of the paramagnetic SiO<sub>2</sub> network formation. TEM images and size distribution of the core and core–shell UCNPs. Schematic of anisotropic shell growth of NaYF<sub>4</sub> shell on the core NaYF<sub>4</sub>; Yb,Er. XRD spectra and SAED pattern of the UCNPs. XPS spectrum, EDX analysis, DLS size distribution and Zeta potential of UCNPs@TEMPO@SiO<sub>2</sub> nanocomposites. Inverted fluorescence microscope images of HeLa cells incubated with nanocomposites. UV-vis spectra of nanocomposites. Geometric structure analysis of UCNPs and the calculation of molar TEMPO radical : molar UCNPs ratio.

See DOI: 10.1039/c4nr07591a

## 1 Introduction

With the development of medical science and technology in recent years, early diagnosis and treatment of diseases is becoming more and more desirable than before. Single imaging techniques used for diagnosis, including magnetic resonance imaging (MRI), ultrasound, X-ray computed tomography (CT), positron emission tomography (PET), single-photon emission CT (SPECT) and optical imaging technologies, are usually insufficient to provide enough information for precise early medical diagnoses and the effective therapy of various diseases. To overcome this shortcoming and incorporate the advantages of different imaging tools, increasing attention has been focused on developing multimodal nanoprobes using combined imaging modalities. One of the frequently reported dual-modal nanoprobes is fabricated by integrating MRI contrast agent and fluorescence probe in a single nanocomposite, which can simultaneously provide excellent three-

dimensional (3D) anatomical and functional information of soft tissues and a high resolution and sensitivity of imaging at the cellular level.<sup>1–4</sup>

The most commonly used fluorescence moieties for MRI/fluorescence dual-modal nanoprobes are organic dyes and semiconductor quantum dots (QDs). However, organic dyes and QDs are downconversion phosphors, their excitation wavelengths are generally within the ultraviolet light or blue light regions. This will lead to a strong autofluorescence background, low penetration depth and damage to biological samples when using them as bioimaging probes. Besides, the photobleaching of organic dyes and the toxicity of QDs also constrains the development of their practical applications as imaging probes. As an alternative to conventional fluorescent probes, lanthanide-doped upconversion nanoparticles (UCNPs) show strong upconversion luminescence (UCL) emission in the near infrared (NIR) or visible range upon irradiation with NIR light. Since the “optical transmission window” of most bio-species is located in the NIR range (750–1000 nm), the use of UCNPs in bioimaging has special advantages including low autofluorescence background, deep tissue penetration and reduced photodamage.<sup>5–9</sup> Considering these valuable advantages, UCNPs are increasingly used as a bioprobe module in multi-modality imaging.<sup>10–12</sup> Co-doping of Gadolinium ( $Gd^{3+}$ ) in the rigid structure of UCNPs is a straightforward strategy to construct dual-modal nanoprobes for UCL/MR dual-modality imaging,<sup>13–20</sup> due to the high paramagnetism property of  $Gd^{3+}$ . However,  $Gd^{3+}$  ions doped deeply inside of the UCNPs have less chance to efficiently exchange magnetic fields with surrounding water protons than those on the surface of nanoparticles.<sup>21</sup> Meanwhile, excessive co-doping of  $Gd^{3+}$  ions can easily cause a quenching of upconversion fluorescence due to the change of host matrix.<sup>22</sup> Thus, core-shell  $NaYF_4$ :Yb, Er/ $NaGdF_4$  nanocrystals were synthesized to improve the longitudinal relaxivity and upconversion luminescence intensity, although it takes a high level of skill to precisely control the thickness of  $NaGdF_4$ .<sup>23</sup> Another strategy to get Gd-UCNP multi-modality bioprobes is to attach a Gd-DTPA complex to the surface of UCNPs.<sup>24,25</sup> However, even for chelated  $Gd^{3+}$ -complexes, the release of the metal ion *in vivo* during metabolic processes and the potential toxicity are pertinent issues, which may cause patient fears and concerns.<sup>13</sup> Besides Gd-based UCNPs, superparamagnetic iron oxide nanoparticles (IONPs) have also been assembled with UCNPs to fabricate multifunctional nanoprobes for UCL/MR imaging.<sup>26,27</sup> However, these IONP-UCNP nanocomposites usually exhibit reduced UCL intensity because the light of excitation and emission could be partially absorbed by the IONPs to some extent.<sup>4</sup> Therefore, it is still challenging and desirable to find some suitable alternatives to Gd-based UCNPs and IONP-UCNP nanocomposites to develop multifunctional nanoprobes for UCL/MR dual-modality imaging.

Nitroxide radicals, such as 2,2,6,6-tetramethylpiperidine 1-oxyl (TEMPO), are a class of stable, non-toxic organic molecules which have a single unpaired electron. Due to their unique paramagnetic property, they have long been used as

spin labelling agents for electron spin resonance (ESR) imaging or as contrast agents for MRI.<sup>28,29</sup> In combination with site-directed spin labeling (SDSL), nitroxide radicals are also well-known as powerful ESR-sensitive probes to study the concentration, structure, dynamics, and interactions of various analytes.<sup>30–32</sup> Because of their ability to participate in cellular redox reactions, nitroxide radicals have also been used as spin probes to monitor redox status *in vivo*.<sup>33,34</sup> As a class of potential MRI contrast-enhancing agents, nitroxide radicals show obvious advantages because of their lower toxicity in comparison with conventional MRI contrast agents (*e.g.*, gadolinium derivatives). However, nitroxide radicals are sensitive to the reduction status of biological samples.<sup>29,33,35</sup> Their rapid *in vivo* reduction to the corresponding diamagnetic hydroxylamines can lead to a significant loss of ESR signal and MRI relaxation time. It has been demonstrated that the half-life of free TEMPO radicals in blood is about 15 s, which is far from satisfactory for practical use.<sup>36</sup> To solve this issue, numerous efforts have been made to enhance the stability of nitroxide radicals by the encapsulation or functionalization of nitroxide radicals into polymers,<sup>37–41</sup> lipid emulsion,<sup>42</sup> DNA oligomers,<sup>43</sup> single-walled carbon nanotubes,<sup>44</sup> and albumin.<sup>45</sup> However, it is still challenging to achieve spin labeled contrast agents with good anti-reduction performance under *in vivo* applications.

Silica coating, chemically and thermally inert against degradation in biological environments, is a frequently used technique for the surface modification of nanoparticles in biomedical applications.<sup>46</sup> This coating method can protect the core nanoparticles against the external environment, thereby improving the stability and biocompatibility of the nanoparticles. Moreover, the silica coated surface of nanoparticles can be further functionalized by biomolecules or ligands with amines, thiols and carboxyl groups.

Inspired by these premises, herein, a TEMPO radicals doped paramagnetic silica layer was coated onto  $NaYF_4$ :Yb, Er/ $NaYF_4$  nanoparticles to construct multifunctional nanoprobes for UCL/MR dual-modality imaging. The as-prepared nanocomposites were labeled as UCNP@TEMPO@ $SiO_2$ , and were further functionalized with poly (ethylene glycol) (PEG) to improve the colloidal stability and biocompatibility. The paramagnetic TEMPO@ $SiO_2$  layer was formed by copolymerization of a paramagnetic precursor (derived from 3-aminopropyltrimethoxysilane (APTS)) with tetraethyl orthosilicate (TEOS). The paramagnetic precursor was obtained by coupling APTS with 4-carboxy-TEMPO. Moreover, this compact inert shell of  $SiO_2$ , acting as a protection barrier, can protect the doped TEMPO radicals from being reduced to the corresponding hydroxylamines by small reducing substances, such as glutathione and ascorbic acid. To the best of our knowledge, this is the first study reporting the novel combination of UCNPs with TEMPO nitroxide radicals for UCL/MR dual-modality imaging. The longitudinal relaxivity of PEGylated UCNP@TEMPO@ $SiO_2$  nanocomposites is about 10 times stronger than that of free nitroxide radicals. MTT assays reveal the low cytotoxicity of the PEGylated UCNP@TEMPO@ $SiO_2$  nanocomposites. This multifunctional nanoprobe was used for *in vitro* UCL bioimaging

under 980 nm infrared laser excitation. In addition, both the  $T_1$ -weighted MRI measurements in an aqueous solution and in a HeLa cells suspension showed the contrast brightening increased with the concentration of PEGylated UCNP@TEMPO@SiO<sub>2</sub> nanocomposites, which revealed that a satisfactory MRI contrast performance of this multifunctional nanoprobe could be obtained. Finally, *in vivo*  $T_1$ -weighted MRI measurements show the enhancement of MR signals in the livers of mice administered with these nanocomposites. These results indicate that the PEGylated UCNP@TEMPO@SiO<sub>2</sub> nanocomposites present potential for UCL/MR dual-modality imaging applications.

## 2 Experimental

### 2.1 Materials

Anhydrous YCl<sub>3</sub> (99.99%), anhydrous YbCl<sub>3</sub> (99.9%), and anhydrous ErCl<sub>3</sub> (99.9%) were purchased from National Engineering Research Centre of Rare Earth Metallurgy and Function Materials (Baotou, China). NaOH (>98%), NH<sub>4</sub>F (>98%), 1-octadecene (ODE, 90%), oleic acid (OA, 90%), and 2-ethoxy-1-ethoxy-carbonyl-1,2-dihydroquinoline (EEDQ) were purchased from Alfa Aesar Co., Ltd (Shanghai, China). Poly-oxyethylene (5) nonylphenylether (Igepal CO-520), 3-aminopropyltrimethoxysilane (APTS), tetraethyl orthosilicate (TEOS), fluorescein isothiocyanate (FITC) and 4-carboxy-TEMPO were purchased from Sigma-Aldrich Co., Ltd (Shanghai, China). mPEG-NHS was purchased from Sinopeg Biotech Co., Ltd (Xiamen, China). Unless otherwise noted, all chemicals were used as received without further purification. Milli-Q water (18.2 MΩ cm) was used in all experiments.

### 2.2 Synthesis of TEMPO@SiO<sub>2</sub> nanoparticles

The core–shell TEMPO@SiO<sub>2</sub> nanoparticles were prepared by a reverse microemulsion approach. Firstly, the silanizing TEMPO radical precursors were prepared by the reaction of 4-carboxy-TEMPO with APTS, which is similar to that reported previously.<sup>47,48</sup> A solution of 22.5 μL of APTS and 24 mg of 4-carboxy-TEMPO with 60.8 mg of EEDQ in methanol (1 mL) was allowed to stand for 24 h at room temperature. After removing methanol *via* reduced pressure distillation, the product was redissolved in 2 mL of water. After ultrasonic dispersion, 150 μL of the solution was mixed with 750 μL of water for further use. TEMPO@SiO<sub>2</sub> was synthesized using a cyclohexane/Triton X-100/*n*-hexanol/water water-in-oil (w/o) reverse microemulsion system. Briefly, cyclohexane (16.8 mL), Triton X-100 (4 mL), and *n*-hexanol (4 mL) were mixed and stirred thoroughly for 10 min, then 150 μL of the as-prepared silanizing TEMPO radical precursors solution was added with continuous stirring for over 5 minutes. Next, the container was sealed and sonicated for 1 h until a transparent emulsion was formed. 60 μL of ammonia (wt 30%) was then added into the solution, and the solution was rotated for 24 h. Thereafter, 100 μL of TEOS was added and the solution was stirred for 12 h. Finally, TEMPO@SiO<sub>2</sub> was precipitated by adding 20 mL

of acetone, and the nanoparticles were washed with acetone and ethanol and dried under vacuum at room temperature.

### 2.3 Synthesis of core NaYF<sub>4</sub>: Yb,Er UCNPs

Monodisperse NaYF<sub>4</sub>:Yb,Er UCNPs were synthesized by a user-friendly one-pot solvothermal strategy using NH<sub>4</sub>F-NaOH–Re-OA as shell precursors. Typically, 0.4 mmol YCl<sub>3</sub>, 0.09 mmol YbCl<sub>3</sub> and 0.01 mmol ErCl<sub>3</sub> in methanol were added to a 100 mL three-neck flask containing 3 mL of OA and 7.5 mL of ODE. The solution was heated to 130 °C under argon flow with constant stirring for 30 min to form a clear yellow solution, and then cooled down to room temperature. 5 mL of methanol solution containing NaOH (0.05 g) and NH<sub>4</sub>F (0.074 g) was added and the solution was stirred for 60 min. After methanol was evaporated, the solution was heated to 300 °C under argon for 1 h and cooled down to room temperature. The obtained UCNPs were precipitated from the solution by adding an equal volume of acetone. The mixed solution was centrifuged at 12 000 rpm for 30 min. The precipitate was then redispersed in a cyclohexane–ethanol–water (2 : 1 : 1) solution. The solution was gently mixed and allowed to stand until the cyclohexane layer did not show any turbidity. The cyclohexane layer containing UCNPs was extracted, then the solvent was removed *via* reduced pressure distillation. The resulting UCNPs with a yield of about 70 mg were redispersed in cyclohexane as a stock solution (10 mg mL<sup>-1</sup>).

### 2.4 Synthesis of core–shell NaYF<sub>4</sub>:Yb,Er/NaYF<sub>4</sub> UCNPs

The synthesis of the core–shell UCNPs was carried out *via* a modified successive layer-by-layer injection protocol. Y-OA precursor: a mixture of YCl<sub>3</sub> (1.75 mmol), OA (5 mL) and ODE (12.5 mL) was added to a flask and heated to 130 °C under vacuum with magnetic stirring for 30 min to form a colorless solution before cooling down to 90 °C for the following injection. NaOH-NH<sub>4</sub>F-OA precursor: first, a mixture of OA (5 mL), ODE (12.5 mL), and 17.5 mL of methanol solution containing NaOH (0.175 g) and NH<sub>4</sub>F (0.259 g) were mixed in a flask. After methanol was evaporated, the solution was heated to 120 °C to remove residual water and oxygen before cooling down to 90 °C for the following injection. The synthesis of core UCNPs was conducted as described above, after reacting for 60 min at 300 °C. Then 0.5 mL of Y-OA precursors and 0.5 mL of NaOH-NH<sub>4</sub>F-OA precursors were successively injected into the reaction mixture and the ripening time between each injection was kept at 15 min. Each injection of shell precursors and ripening cycles represented a layer growth. The injection could be performed for 15 cycles and 30 cycles to get core–shell UCNPs with 15 layers and 30 layers, respectively. The resulting core–shell UCNPs were collected and washed by the same method as mentioned above.

### 2.5 Synthesis of UCNP@TEMPO@SiO<sub>2</sub> nanocomposites

UCNP@TEMPO@SiO<sub>2</sub> nanocomposites were synthesized using a cyclohexane/CO-520/water water-in-oil (w/o) reverse microemulsion system. 0.45 mL of CO-520, 2 mL of cyclohexane and 1 mL of 10 mg mL<sup>-1</sup> NaYF<sub>4</sub>:Yb,Er/NaYF<sub>4</sub> solution in cyclo-

hexane were mixed and stirred for 15 min, 50  $\mu\text{L}$  of ammonia (wt 30%) was added dropwise, and the container was sealed and sonicated for 1 h until a transparent emulsion was formed. The silanizing TEMPO radical precursors in methanol (1 mL) were condensed to 100  $\mu\text{L}$ . Then, 50  $\mu\text{L}$  of silanizing TEMPO radical precursors in methanol was added into the reverse microemulsion solution. The solution was magnetically stirred (600 rpm) for 12 h. After that, 20  $\mu\text{L}$  of TEOS and 3  $\mu\text{L}$  of APTS were added and the reaction was kept for another 12 h. Finally, the nanoparticles were obtained by centrifugation and washed with ethanol–water (1 : 1) thoroughly and then stored in deionized water.

## 2.6 Synthesis of PEGylated UCNP@TEMPO@SiO<sub>2</sub> nanocomposites

Briefly, the purified UCNP@TEMPO@SiO<sub>2</sub>-NH<sub>2</sub> (20 mg) nanoparticles were dispersed in 4 mL of DMF, and 20 mg of mPEG-NHS was added for the PEGylation of nanoparticles. After 12 h of reaction, the PEGylated UCNP@TEMPO@SiO<sub>2</sub> nanocomposites were collected by centrifugation and washed with deionized water several times and then stored in deionized water.

## 2.7 Characterization

Powder X-ray diffraction (XRD) was performed on an AXS D8 advance (Bruker, Germany). Transmission electron microscopy (TEM) images were obtained using a JEM-1400 (JEOL, Japan). High-resolution TEM (HRTEM), selected-area electron diffraction (SAED), and energy-dispersive X-ray (EDX) analysis were performed on a TECNAI F-30 (FEI, Netherlands). X-ray photo-electron (XPS) measurements were performed on a PHI Quantum 2000 XPS system (ULVAC-PHI Inc., Japan). Upconversion luminescence emission spectra were collected on a FluoroMax-4 spectrometer (Jobin Yvon Horiba, France) equipped with the excitation of an external 0–2 W adjustable 980 nm CW laser (Beijing Hi-tech Optoelectronic Co., China). Dynamic light scattering (DLS) and Zeta potential distribution were measured on a Malvern Zetasizer Nano ZS (Malvern, UK). The upconversion luminescence (UCL) imaging was performed on a modified Nikon Ti-S inverted fluorescence microscope (Nikon, Japan) equipped with an external 980 nm CW laser (Beijing Hi-tech Optoelectronic Co., China). The MR  $T_1$  relaxation and MR  $T_1$ -weighted imaging measurements were performed on a 9.4 T MR scanner (Bruker 94/20, Germany). Flow cytometry analysis was performed on a BD Accuri C6 flow cytometer (BD Biosciences, USA). ESR measurements were performed using a Bruker EMX X-Band ESR spectrometer (Bruker, Germany). All microwave parameters were kept constant: 9.8 GHz microwave frequency, 2.0 mW microwave power, 10 dB attenuator, 100 kHz modulation frequency, 1.0 G modulation amplitude, and 0.64 ms time constant. The Fourier Transform Infrared (FTIR) spectra were recorded on a Nicolet iS10 (Thermo Scientific, USA). The concentration of samples was fixed *via* the measurement of the Yb<sup>3+</sup> content in each sample by inductively coupled plasma atomic emission spectroscopy (ICP-AES).

## 2.8 Cell culture and cytotoxicity assay

HeLa cells were a kind gift from the Medical College of Xiamen University. Cells were cultured in DMEM (Dulbecco's Modified Eagle Medium) supplemented with 10% FBS, 1% penicillin/streptomycin and 2 mM L-glutamine, at 37 °C in a 5% CO<sub>2</sub> humidified atmosphere. The *in vitro* cytotoxicity was measured by using a 3-(4,5-dimethylthiazol-2-yl)-2,5-diphenyltetrazolium bromide (MTT) assay on HeLa cells. According to the typical procedure, HeLa cells were seeded into a 96-well culture plate at 1 × 10<sup>4</sup> cells per well and cultured in 5% CO<sub>2</sub> at 37 °C for 24 h. The cells were subsequently incubated with various concentrations (6.25, 12.5, 25, 50, 100, 200 and 400  $\mu\text{g}$  mL<sup>-1</sup>, diluted in DMEM) of PEGylated UCNP@TEMPO@SiO<sub>2</sub> nanocomposites for 6 h or 24 h. Thereafter, the cells were washed three times with phosphate-buffered saline (PBS) and incubated with MTT solution (1 mg mL<sup>-1</sup>) at 37 °C in 5% CO<sub>2</sub> for 4 h. After the growth medium was removed, 100  $\mu\text{L}$  of dimethyl sulfoxide (DMSO) was added in each well followed by incubation for another 30 min. Finally the absorbance of the resulting solution was measured at 570 nm using a microplate reader (BioRad 680, Hercules, CA, USA). The cell viability was displayed as a percentage of the control samples.

$$\text{Cell viability}(\%) = [A]_{\text{sample}}/[A]_{\text{control}} \times 100\%$$

where [A]<sub>sample</sub> is the absorbance of formazan product in treated cells and [A]<sub>control</sub> is the absorbance of formazan in untreated cells.

## 2.9 Cellular uptake assay

The cellular uptake of PEGylated UCNP@TEMPO@SiO<sub>2</sub> was analyzed by flow cytometry. The as-prepared UCNP@TEMPO@SiO<sub>2</sub>-NH<sub>2</sub> nanocomposites were labeled with FITC and mPEG-NHS. Briefly, 25 mg of UCNP@TEMPO@SiO<sub>2</sub>-NH<sub>2</sub> was dispersed in 20 mL of DMF, then, 20 mg of mPEG-NHS was added. The solution was magnetically stirred (600 rpm) for 12 h. After that, a certain amount of FITC was added and stirred overnight. The resulting FITC-labeled PEGylated UCNP@TEMPO@SiO<sub>2</sub> was centrifuged and washed with ethanol several times. HeLa cells were seeded into 12-well plates at 1 × 10<sup>5</sup> cells per well and incubated with samples (0, 8, 15, 30, 60, 125  $\mu\text{g}$  mL<sup>-1</sup>) at 37 °C in 5% CO<sub>2</sub> for 6 h, and then washed with PBS sufficiently to remove excess nanocomposites. After that, the cells were collected by trypsinization and suspended in PBS. Cells incubated in the absence of the UCNPs were used as a control. The amounts of samples taken up by cells were measured using the FL-1 channel. FACS data were analyzed using Flow Jo (version 7.6).

## 2.10 Upconversion luminescence bioimaging *in vitro*

Upconversion luminescence imaging was performed on an inverted fluorescence imaging microscope (Nikon Ti-S) equipped with an external CW 980 nm laser as the excitation source. An 850 nm short-pass filter was placed before the CCD to cut the excitation light. HeLa cells grown on coverslips (1 × 10<sup>5</sup> per well) were incubated with PEGylated UCNP@TEM-

$\text{PO}@\text{SiO}_2$  (0, 40, 80, 120, 160, 200  $\mu\text{g mL}^{-1}$ ) at 37 °C in 5%  $\text{CO}_2$  for 6 h. After washing three times with PBS, the cells were also stained with Hoechst 33258 (50  $\mu\text{g mL}^{-1}$ ) for 30 min to show the nuclei as blue. After washing with PBS again for three times, the upconversion luminescence signals were collected at 500–560 nm with 3 s of exposure by a 20 $\times$  objective lens.

### 2.11 MRI of PEGylated UCNP@TEMPO@SiO<sub>2</sub> *in vitro*

The MR  $T_1$  relaxation and MR  $T_1$ -weighted imaging measurements were performed on a 9.4 T MR scanner (Bruker 94/20, Germany). Firstly, different amounts of PEGylated UCNP@TEMPO@SiO<sub>2</sub> nanocomposites were prepared in a series of equal volume aqueous solutions with 1% agarose gel in 200  $\mu\text{L}$  PCR tubes (0, 0.313, 0.625, 1.25, 2.5, 5  $\text{mg mL}^{-1}$ ) for MR  $T_1$  relaxation and MR  $T_1$ -weighted imaging measurements. Secondly, HeLa cells were incubated with different concentrations (0, 40, 80, 120, 160, 200  $\mu\text{g mL}^{-1}$ ) of PEGylated UCNP@TEMPO@SiO<sub>2</sub> nanocomposite for 6 h. The labeled cells were washed with PBS, then collected by trypsinization and suspended in a series of equal volumes of DMEM culture media with 1% agarose gel in 200  $\mu\text{L}$  PCR tubes before MR  $T_1$  relaxation measurement. Unlabeled cells were used as the control group.

### 2.12 MRI of PEGylated UCNP@TEMPO@SiO<sub>2</sub> *in vivo*

Animal experiment procedures were in agreement with the protocol approved by the Institutional Animal Care and Use Committee of Xiamen University. For *in vivo* MRI studies, nude mice were anesthetized by intraperitoneal injection of sodium pentobarbital (40 mg  $\text{kg}^{-1}$ ). In order to raise the signal to noise ratio, a commercially available volume coil (RF RES 1H 75/40 Q TR, Germany) with 40 mm diameter was used. After intravenous injection of PEGylated UCNP@TEMPO@SiO<sub>2</sub> nanoparticles (200  $\mu\text{L}$ , 0.5  $\text{mg mL}^{-1}$ ), coronal and transversal cross section MR imaging was performed on a 9.4 T MR

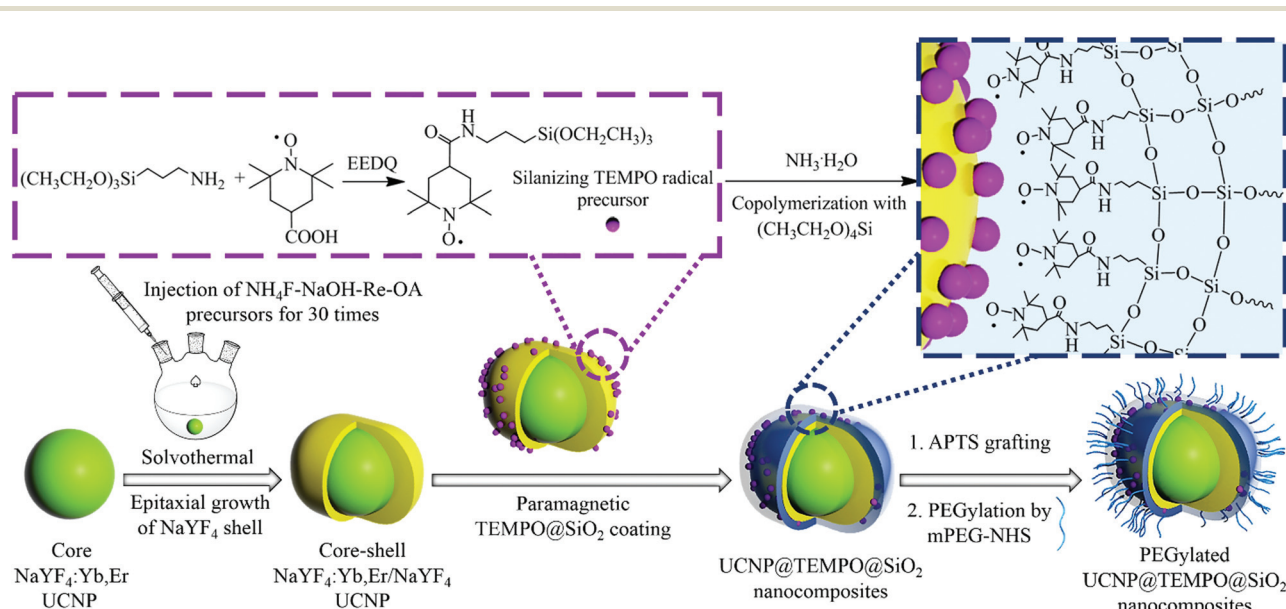
scanner (TR = 1500 ms, TE = 8.5 ms, FOV 4 cm × 4 cm, slice thickness 1 mm). The MR images were obtained at baseline (prior to injection) and at 30 min post-injection. The animals were then removed from the MR scanner and allowed to recover.

## 3 Results and discussion

PEGylated UCNP@TEMPO@SiO<sub>2</sub> nanocomposites were constructed by the novel combination of homogenous active core-inert shell UCNPs and nitroxide radicals. As shown in Scheme 1, the synthetic procedures for PEGylated UCNP@TEMPO@SiO<sub>2</sub> nanocomposites were divided into three steps. Firstly, uniformly sized active core-inert shell NaYF<sub>4</sub>:Yb,Er/NaYF<sub>4</sub> with strong UCL emission was synthesized by a user-friendly one-pot solvothermal strategy using NH<sub>4</sub>F-NaOH-Re-OA as shell precursors. Thereafter, 4-carboxyl TEMPO was conjugated with APTS to get a silanizing TEMPO radical. For transferring the hydrophobic UCNPs to an aqueous solution, the paramagnetic TEMPO@SiO<sub>2</sub> layer was coated on the surface of UCNPs by copolymerization with the silanizing TEMPO radical and TEOS *via* a reverse microemulsion method. Finally, in order to increase the colloidal stability and biocompatibility, mPEG-NHS was linked with the amino-functionalized SiO<sub>2</sub> on the surface of UCNP@TEMPO@SiO<sub>2</sub>. These as-prepared PEGylated UCNP@TEMPO@SiO<sub>2</sub> nanocomposites could serve as effective multifunctional nanoprobes for UCL/MR multi-modal bioimaging.

### 3.1 Synthesis and characterization of TEMPO@SiO<sub>2</sub> nanoparticles

Firstly, we took TEMPO@SiO<sub>2</sub> nanoparticles as a model to test whether the compartmentalization of the TEMPO radicals in



Scheme 1 Schematic illustration of the synthesis of the PEGylated UCNP@TEMPO@SiO<sub>2</sub> nanocomposites.

the core of  $\text{SiO}_2$  nanoparticles could enhance the stability of their ESR signal under a reducing environment. The silanizing TEMPO radical precursors were obtained by a coupling reaction which has the advantage of high yield. 4-Carboxy-TEMPO was conjugated to APTS in the presence of EEDQ, yielding the desired silanizing TEMPO radical (Scheme 1). This successful conjugation was confirmed by the measurement of FTIR (Fig. S1†) and ESI-MS (Fig. S2†) spectra. Then, the paramagnetic  $\text{TEMPO}@\text{SiO}_2$  nanoparticles were synthesized by copolymerization of silanizing TEMPO radicals with TEOS in reverse microemulsion. As shown in Fig. S3,† the obtained  $\text{TEMPO}@\text{SiO}_2$  nanoparticles are roughly spherical with an average diameter of  $33.5 \pm 2.4$  nm. The ESR signals of the obtained silanizing TEMPO radical precursors (Fig. S4a†) and  $\text{TEMPO}@\text{SiO}_2$  nanoparticles (Fig. S4b†) were then analyzed by ESR measurement. The ESR spectrum of the silanizing TEMPO radical precursors shows the expected three  $^{14}\text{N}$  hyperfine lines, which are characteristic of freely-tumbling TEMPO radicals in solution. Moreover, the high-field line is slightly weaker than the others, indicating the slower tumbling rate of the TEMPO molecule, due to the covalent attachment with an APTS moiety (Fig. S4a†). In contrast, the ESR spectrum of the  $\text{TEMPO}@\text{SiO}_2$  nanoparticles exhibits distinct anisotropy as evidenced by the broader line-width and the weaker high-field line than that of silanizing TEMPO radicals (Fig. S4b†). Fig. S5† shows the formation process of the paramagnetic silica network structure, in which the silanizing TEMPO radicals stay at a very close distance to each other. The restriction of the mobility of TEMPO radicals embedded into a rigid  $\text{SiO}_2$  network structure can lead to a broadening of the ESR linewidth and to a lower relative intensity of the high field signal,<sup>37,49</sup> possibly due to the slower molecular tumbling. Furthermore, the high population of TEMPO radicals, which stay at a very close distance to each other in this self-assembling  $\text{SiO}_2$  structure, may also lead to the broadness of ESR lines, due to the spin–spin interaction.<sup>37,50</sup> In addition, no noticeable ESR signal was observed in the supernatant after centrifugation of the solutions of  $\text{TEMPO}@\text{SiO}_2$  (Fig. S4c†). In order to further prove that the TEMPO radicals were covalently attached to the  $\text{SiO}_2$  nanoparticles, we carried out control experiments by simply mixing the APTS and 4-carboxy-TEMPO as precursors during the co-hydrolysis process. Without the covalent linkage between APTS and 4-carboxy-TEMPO, TEMPO radicals may only adhere to  $\text{SiO}_2$  nanoparticles by physical adsorption. After several rounds of centrifugation and washing, no ESR signal could be observed in the final product of  $\text{SiO}_2$  nanoparticles (Fig. S4d†). The results of these control experiments show that the ESR signal of  $\text{TEMPO}@\text{SiO}_2$  was originated from the TEMPO radicals covalently immobilized within the  $\text{SiO}_2$  nanoparticles, instead of those encapsulated by physical adsorption.

As mentioned above, nitroxide radicals are sensitive to the reduction environment of biological systems. Antioxidants such as ascorbic acid (Vc) and glutathione (GSH) are vital to maintain the redox status in living cells and widely exist *in vivo*. Meanwhile, there is a higher concentration of Vc in the blood and the reduction of nitroxide radicals into the corres-

ponding hydroxylamines by GSH is much slower than Vc.<sup>51</sup> Thus, we compared the reduction resistance of TEMPO radicals embedded in the  $\text{TEMPO}@\text{SiO}_2$  nanoparticles with the free TEMPO radicals in the presence of the antioxidant Vc.

The time-course of ESR signal intensity of  $\text{TEMPO}@\text{SiO}_2$  nanoparticles and free TEMPO radicals is shown in Fig. 1. The ESR signal of the as-prepared  $\text{TEMPO}@\text{SiO}_2$  was not significantly affected by ascorbic acid up to a concentration of 5 mM while the signal intensity of free TEMPO radicals decreased rapidly within about 1 min. These results indicate that the compact network structure of  $\text{SiO}_2$  could act as both a protector and a promising carrier of nitroxide radicals, the compartmentalization of the TEMPO radicals in the microstructure of  $\text{SiO}_2$  nanoparticles is an effective way to maintain their ESR signal, especially in a reducing environment.

In addition, the reduction resistance of  $\text{TEMPO}@\text{SiO}_2$  was also confirmed by time-course MRI. The time-courses of  $T_1$ -weighted MR images of  $\text{TEMPO}@\text{SiO}_2$  nanoparticles and free TEMPO radicals under a reducing environment are shown in Fig. 2. Compared with the Tris-HCl buffer blank control, both

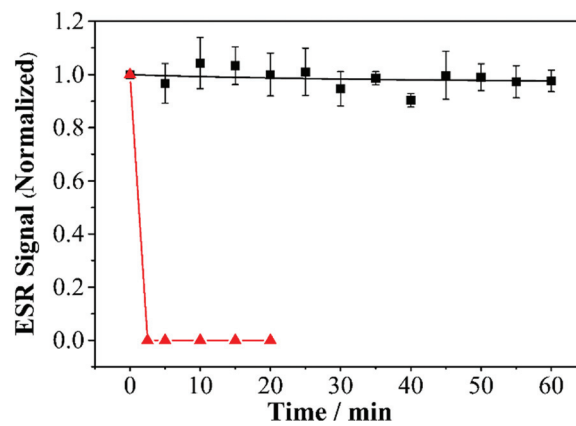


Fig. 1 Time-course of ESR signal intensity of  $\text{TEMPO}@\text{SiO}_2$  nanoparticles (■) and 4-hydroxyl-TEMPO (▲) in the presence of 5 mM ascorbic acid. (Performed in 20 mM pH 7.4 Tris-HCl buffer solution, [4-hydroxyl-TEMPO] = 10 mM,  $\text{TEMPO}@\text{SiO}_2$  nanoparticles: 7 mg mL<sup>-1</sup>.)

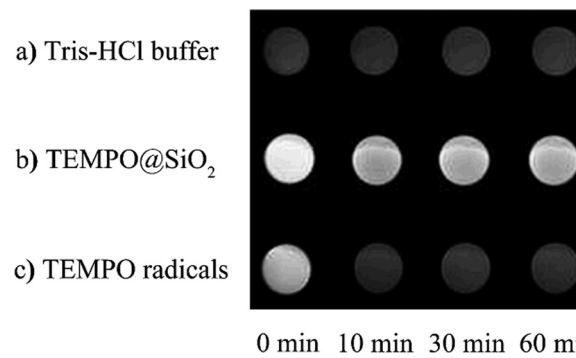


Fig. 2 Time-course of  $T_1$ -weighted MR images for (a) Tris-HCl buffer control, (b)  $\text{TEMPO}@\text{SiO}_2$  nanoparticles and (c) 4-hydroxyl-TEMPO in the presence of 5 mM ascorbic acid. (Performed in 20 mM pH 7.4 Tris-HCl buffer solution, [4-hydroxyl-TEMPO] = 1 mM,  $\text{TEMPO}@\text{SiO}_2$  nanoparticles: 7 mg mL<sup>-1</sup>.)

TEMPO@SiO<sub>2</sub> nanoparticles and free TEMPO radicals showed significant contrast enhancement of *T*<sub>1</sub>-weighted MRI in Tris-HCl solution containing Vc (5 mM) at the very start. By virtue of the compact network structure of SiO<sub>2</sub>, the TEMPO radicals embedded in TEMPO@SiO<sub>2</sub> nanoparticles could resist reduction for 1 h, while the contrast enhancement of free TEMPO radicals decreased quickly within 10 min, which is ascribed to their reduction by Vc.

### 3.2 One-pot synthesis and characterization of core NaYF<sub>4</sub>:Yb, Er and core–shell NaYF<sub>4</sub>:Yb,Er/NaYF<sub>4</sub> UCNPs

TEM images of core NaYF<sub>4</sub>:Yb,Er and core–shell NaYF<sub>4</sub>:Yb,Er/NaYF<sub>4</sub> nanoparticles are shown in Fig. 3. All of these nanoparticles were orderly self-assembled on the TEM grid easily (Fig. S6†). As can be seen in Fig. 3(a), the core NaYF<sub>4</sub>:Yb,Er nanoparticles are uniform and nearly spherical in shape with an average diameter of  $19.6 \pm 1.1$  nm. The morphology of the resulting core–shell NaYF<sub>4</sub>:Yb,Er/NaYF<sub>4</sub> nanoparticles coated with 15 layers (Fig. 3b) and 30 layers (Fig. 3c) of NaYF<sub>4</sub> shell became ellipsoidal in shape with a narrow size distribution and the average size increased from  $19.6 \pm 1.1$  nm (core size) to  $27.2 \pm 1.1$  nm (length)  $\times$   $21.7 \pm 0.9$  nm (width) and  $33.4 \pm 1.2$  nm  $\times$   $25.1 \pm 1.1$  nm, respectively. Meanwhile, the corresponding high-resolution TEM (HRTEM) images of core NaYF<sub>4</sub>:Yb,Er (Fig. 3e) and core–shell NaYF<sub>4</sub>:Yb,Er/NaYF<sub>4</sub> (Fig. 3f and g) reveal the high crystallinity of these nanoparticles. The distances between lattice fringes were 0.520 nm and 0.299 nm, consistent with the (100) and (110) lattice planes of hexagonal-phase NaYF<sub>4</sub> structure, respectively. All core and core–shell samples were further determined as hexagonal phase NaYF<sub>4</sub>

by XRD (Fig. S9†) and SAED (Fig. S10†). This shape variation from spherical to ellipsoidal nanoparticles further confirms the successively epitaxial growth of an inert NaYF<sub>4</sub> layer due to anisotropic shell growth (Fig. S7†). It can therefore be concluded from these observations that the growth of the NaYF<sub>4</sub> shell on core NaYF<sub>4</sub>:Yb,Er is highly anisotropic (Fig. S8†). In addition, the approximate volume ratio of core NaYF<sub>4</sub>:Yb,Er to outer NaYF<sub>4</sub> shell is 1 : 3.19. This value is consistent with the molar ratio of the precursors of lanthanide input (1 : 3) for generating the core and shell components, respectively. (The detailed geometric structures analysis is presented in the ESI.†)

Upconversion luminescence (UCL) spectra of core NaYF<sub>4</sub>:Yb,Er nanoparticles and core–shell NaYF<sub>4</sub>:Yb,Er/NaYF<sub>4</sub> nanoparticles are shown in Fig. 4. Under 980 nm laser excitation, a set of upconversion emissions centered at 379 nm, 410 nm, 521 nm, 542 nm and 651 nm are observed, corresponding to the  $^4G_{11/2} \rightarrow ^4I_{15/2}$  (379 nm),  $^2H_{9/2} \rightarrow ^4I_{15/2}$  (410 nm),  $^2H_{11/2} \rightarrow ^4I_{15/2}$  (521 nm),  $^4S_{3/2} \rightarrow ^4I_{15/2}$  (542 nm), and  $^4F_{9/2} \rightarrow ^4I_{15/2}$  (651 nm) transitions of Er<sup>3+</sup> ions, respectively.<sup>52</sup> The total integrated UCL intensity of core–shell NaYF<sub>4</sub>:Yb,Er/NaYF<sub>4</sub> nanoparticles with successive shell growth showed an obvious enhancement, even up to a factor of about 60 times for the core–shell NaYF<sub>4</sub>:Yb,Er/NaYF<sub>4</sub> nanoparticles with 30 layers of NaYF<sub>4</sub> shell (Fig. S11†). This result suggests that epitaxial growth of multiple inert NaYF<sub>4</sub> shells on the core NaYF<sub>4</sub>:Yb,Er nanoparticles can effectively minimize the luminescence quenching from the imperfections located at the core particle surface and the surrounding ligands and solvents with high phonon energy.<sup>53</sup>

Compared with the one-pot successive layer-by layer (LBL) thermal decomposition method developed by Zhao *et al.* (the

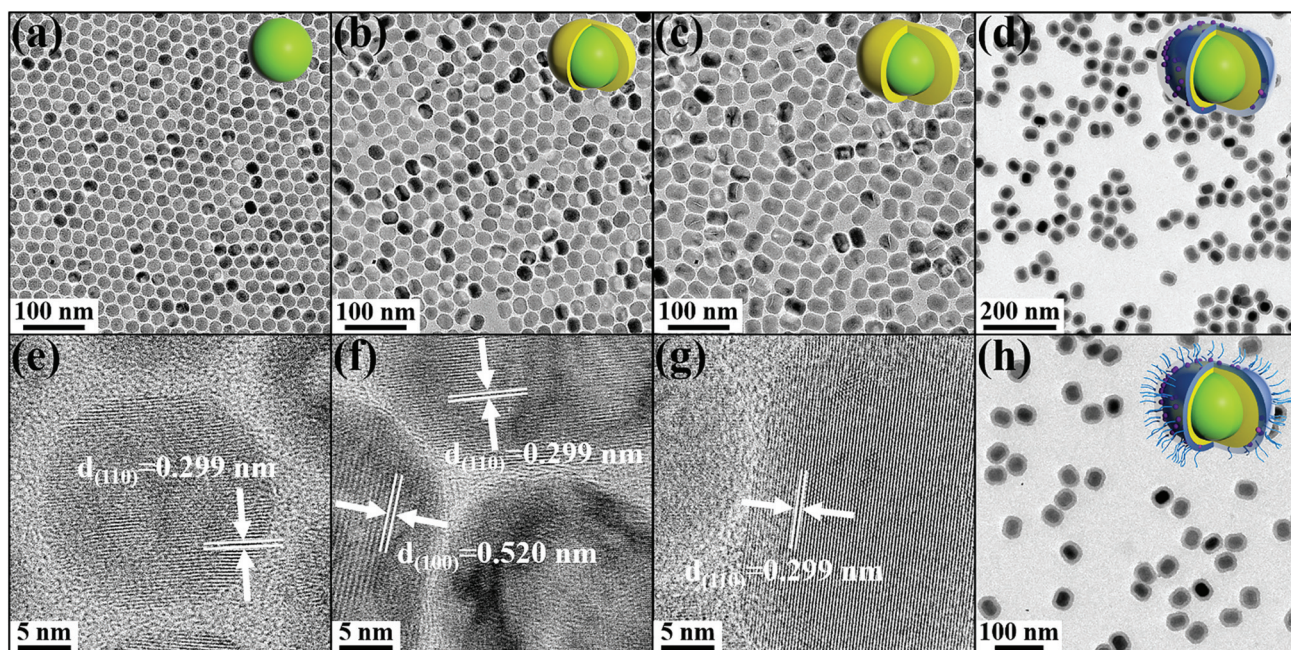
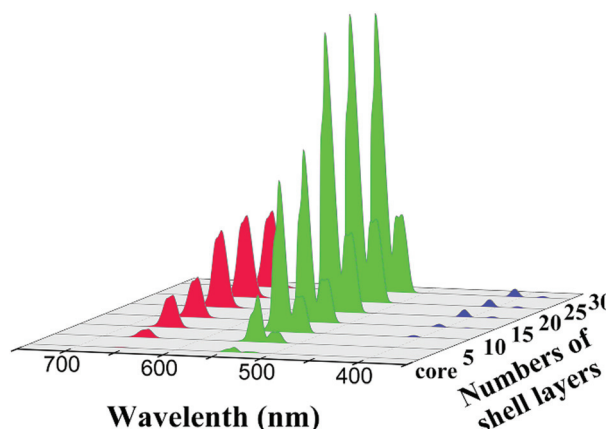


Fig. 3 TEM images of core NaYF<sub>4</sub>:Yb,Er nanoparticles (a), core–shell NaYF<sub>4</sub>:Yb,Er/NaYF<sub>4</sub> nanoparticles with 15 (b) and 30 (c) layers of NaYF<sub>4</sub> shell, UCNP@TEMPO@SiO<sub>2</sub> nanocomposites (d) and PEGylated UCNP@TEMPO@SiO<sub>2</sub> nanocomposites (h). (e)–(g) show the corresponding HRTEM images of (a)–(c), respectively.



**Fig. 4** Upconversion emission spectra of the core  $\text{NaYF}_4\text{:Yb,Er}$  and core–shell  $\text{NaYF}_4\text{:Yb,Er}/\text{NaYF}_4$  UCNPs with different layers of inner  $\text{NaYF}_4$  shell at the same concentration ( $1 \text{ mg mL}^{-1}$ ) in cyclohexane under  $980 \text{ nm}$  excitation (power  $0.1 \text{ W}$ ).

molar concentration ratio of  $\text{F}^-/\text{Ln}^{3+}$  ions is  $6:1$ <sup>54</sup> and Chen *et al.* (the molar concentration ratio of  $\text{F}^-/\text{Ln}^{3+}$  ions is  $12:1$ )<sup>55</sup>, it has to be mentioned that we still choose a stoichiometric amount of  $\text{NaOH}$  and  $\text{NH}_4\text{F}$  mixed with lanthanide–oleate coordination complexes in OA/ODE dispersion as the shell precursor (the molar concentration ratio of  $\text{F}^-/\text{Ln}^{3+}$  ions is  $4:1$ ), owing to some safety concerns about the HF gas or toxic fluorinated species produced by the pyrolysis of excessive fluoride reactants ( $\text{CF}_3\text{COONa}$ ,  $(\text{CF}_3\text{COO})_3\text{Re}$ , etc.) at high temperatures. By this user-friendly one-pot solvothermal strategy using  $\text{NH}_4\text{F}-\text{NaOH}-\text{Re}-\text{OA}$  as shell precursors, the injection could be easily performed to more than 50 cycles to prepare hierarchical uniform core–shell UCNPs, without worrying about excess amounts of fluoride reactants in the high temperature reaction.

### 3.3 Synthesis and characterization of PEGylated UCNP@TEMPO@SiO<sub>2</sub> nanocomposites

Inspired by the high reduction resistance of TEMPO@SiO<sub>2</sub> against reducing environments, we further developed a hybrid nanocomposite by using core–shell  $\text{NaYF}_4\text{:Yb,Er}/\text{NaYF}_4$  (30 layers) UCNPs as the core and the TEMPO@SiO<sub>2</sub> as the shell, which could maintain the ESR signal under reducing conditions for a long time when these nanocomposites were used in UCL/MR dual-modality imaging. At the same time, the TEMPO@SiO<sub>2</sub> would serve as a hydrophilic shell to make the hydrophobic  $\text{NaYF}_4\text{:Yb,Er}/\text{NaYF}_4$  UCNPs dispersible in aqueous solution and easy to functionalize with various biomolecules. A TEM image of the  $\text{NaYF}_4\text{:Yb,Er}/\text{NaYF}_4$  nanoparticles coated with a TEMPO@SiO<sub>2</sub> shell is shown in Fig. 3d. It confirms the successful preparation of monodisperse UCNP@TEMPO@SiO<sub>2</sub> nanocomposites. The thickness of the TEMPO@SiO<sub>2</sub> shell was about 10 nm. The narrow size distribution also indicates the uniform morphology of the UCNP@TEMPO@SiO<sub>2</sub> nanocomposites (length:  $51.8 \pm 1.6 \text{ nm}$ , width:  $43.9 \pm 1.7 \text{ nm}$ ). X-ray photoelectron (XPS) spectra analysis provides detailed information on the chemical composition of the

UCNP@TEMPO@SiO<sub>2</sub> nanocomposites (Fig. S12†). The wide scan spectrum indicates the presence of Si, Y, C, N, O, F and Na elements in the UCNP@TEMPO@SiO<sub>2</sub> nanocomposites. This chemical composition was also confirmed by EDX analysis (Fig. S13†).

Next, the obtained UCNP@TEMPO@SiO<sub>2</sub> nanocomposites were transferred to a capillary tube, followed by ESR measurement. As shown in Fig. 5, the ESR lines of the UCNP@TEMPO@SiO<sub>2</sub> nanocomposites were extensively broader than that of the TEMPO@SiO<sub>2</sub> nanoparticles. The mobility restriction accompanying the binding of TEMPO radicals to UCNPs@SiO<sub>2</sub> may contribute to the broadening of the ESR spectra. On the other hand, the ESR signal of UCNP@TEMPO@SiO<sub>2</sub> nanocomposites was gradually enhanced with the increase of the loading content of TEMPO radicals in the SiO<sub>2</sub> shell. The DLS data of the UCNP@TEMPO@SiO<sub>2</sub> nanocomposites indicates that these nanoparticles are uniform in size and well dispersed in aqueous solution (Fig. S14†). A slight increase of the hydrodynamic size could be caused by an increase of the amount of the silanizing TEMPO radical precursors added during the process of copolymerization. Then, APTS was used to further modify the surface of UCNP@TEMPO@SiO<sub>2</sub> to provide active amino-groups for the graft of PEG or target molecules. In order to improve biocompatibility and extend blood circulation time, mPEG-NHS was immobilized to the surface of UCNP@TEMPO@SiO<sub>2</sub>-NH<sub>2</sub>. Note that the PEG derivative modification on the outermost surface of UCNP@TEMPO@SiO<sub>2</sub> has no obvious effect on the morphology and size of the nanocomposites, as shown in the corresponding TEM images (Fig. 3d and h). However, these surface modifications can substantially affect the surface zeta potentials of the involved nanocomposites (Fig. S15†). The UCNP@TEMPO@SiO<sub>2</sub> nanocomposites initially hold a zeta potential of  $-36.1 \text{ mV}$ . After modifying with APTS, the zeta potential increased to  $+27.2 \text{ mV}$ , and then reduced to  $+22.8 \text{ mV}$  after PEGylation. The reverse of zeta potential from negative to positive is attributed to the introduction of positive primary amine groups, however the

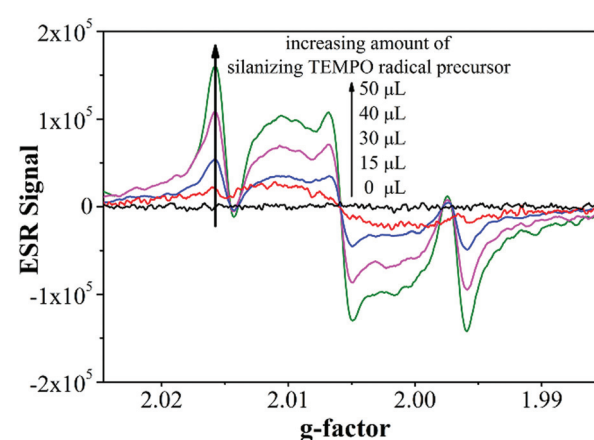


**Fig. 5** The ESR spectra recorded in aqueous solution of the UCNP@TEMPO@SiO<sub>2</sub> nanocomposites synthesized with variable amounts of silanizing TEMPO radical precursors added during the process of copolymerization.

decrease of zeta potential from +27.2 mV to +22.8 mV is attributed to the consumption of positive amine groups on the surface of the nanocomposites during the PEGylation process. Furthermore, the hydrodynamic diameter of the UCNP@TEMPO@SiO<sub>2</sub>-PEG (78.8 nm) is larger than that of UCNP@TEMPO@SiO<sub>2</sub> (60.8 nm), which was attributed to the formation of protective layers of PEG bound covalently to the surface of the UCNP@TEMPO@SiO<sub>2</sub>. The obtained PEGylated UCNP@TEMPO@SiO<sub>2</sub> nanocomposites can be well dispersed in serum for 24 h at 37 °C (data not shown), which will extend their blood circulation time.

In order to test whether the multifunctional nanoprobes can maintain a satisfactory paramagnetic property in a reducing environment, we evaluated the reduction resistance capacity of PEGylated UCNP@TEMPO@SiO<sub>2</sub> nanocomposites in the presence of ascorbic acid. The time-courses of the ESR signal intensity of the as-prepared PEGylated UCNP@TEMPO@SiO<sub>2</sub> nanocomposites and free TEMPO radicals are shown in Fig. 6. When the free TEMPO radicals solution was monitored in the presence of 5 mM ascorbic acid, the signal intensity rapidly decreased within a minute. On the contrary, the ESR signal intensity of the PEGylated UCNP@TEMPO@SiO<sub>2</sub> nanocomposites maintained at a stable level for more than 60 min, indicating that the TEMPO radicals in PEGylated UCNP@TEMPO@SiO<sub>2</sub> nanocomposites resisted reduction even in the presence of 5 mM ascorbic acid. The high stability of the TEMPO radicals in the nanocomposite system means that signal will be observed for a long time and these nanocomposites are promising as new multifunctional nanoprobes for UCL/MR dual-modality imaging.

In order to assess the feasibility of the as-prepared nanocomposites for bioimaging applications, the upconversion luminescence (UCL) spectra of (a) core-only and (b) core-shell UCNP in cyclohexane, (c) UCNP@SiO<sub>2</sub> nanocomposites and (d) PEGylated UCNP@TEMPO@SiO<sub>2</sub> nanocomposites in deionized water, are shown in Fig. 7. Here the UCNP refers to the core-shell NaYF<sub>4</sub>:Yb,Er/NaYF<sub>4</sub> (30 layers).

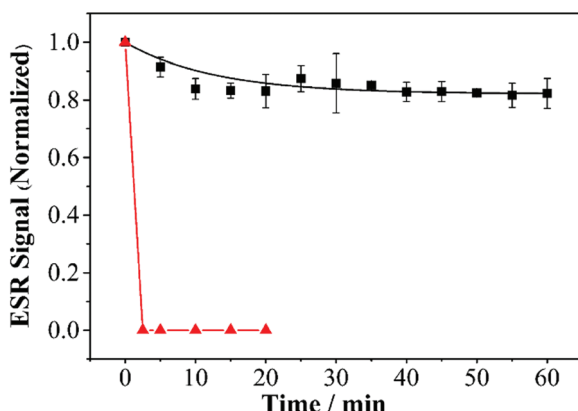


Fig. 6 Time-course of ESR signal intensity of UCNP@TEMPO@SiO<sub>2</sub> nanocomposites (■, 15 mg mL<sup>-1</sup>, synthesized with 50 μL silanizing TEMPO radical precursors) and 4-hydroxyl-TEMPO (▲, 10 mM) in the presence of 5 mM ascorbic acid. (Performed in 20 mM pH 7.4 Tris-HCl buffer solution.)

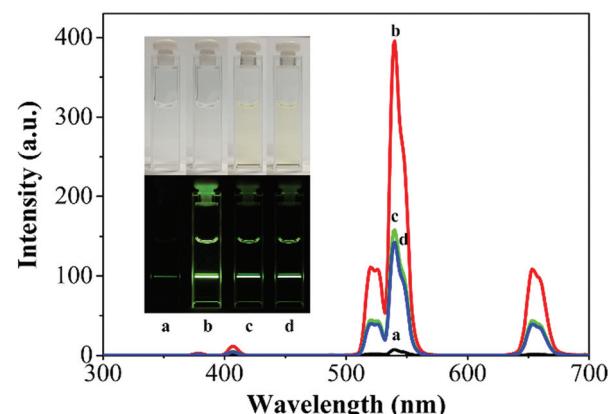
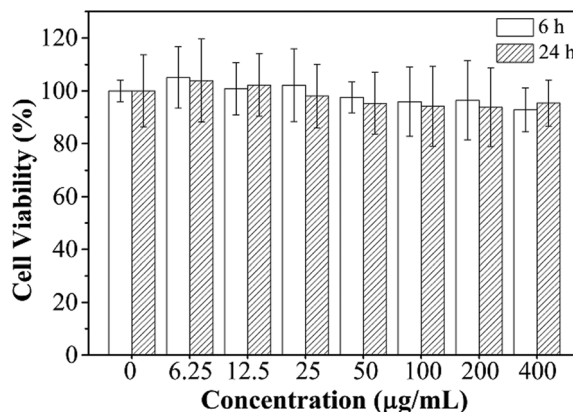


Fig. 7 Upconversion luminescence spectra of (a) core NaYF<sub>4</sub>:Yb,Er and (b) core-shell NaYF<sub>4</sub>:Yb,Er/NaYF<sub>4</sub> in cyclohexane, (c) UCNP@SiO<sub>2</sub> nanocomposites and (d) PEGylated UCNP@TEMPO@SiO<sub>2</sub> nanocomposites in deionized water. Here the UCNP refers to the core-shell NaYF<sub>4</sub>:Yb,Er/NaYF<sub>4</sub> (30 layers). The inset shows photographs of the upconversion emission of the corresponding solution in the daylight (top) and in the dark (bottom) under excitation of 980 nm (power 0.6 W).

the core-shell NaYF<sub>4</sub>:Yb,Er/NaYF<sub>4</sub> (30 layers). All of the spectra were obtained with same concentration of Yb<sup>3+</sup> in sample solution as measured by ICP-AES. Compared with the core-shell UCNP in cyclohexane, the UCL intensity of the UCNP@SiO<sub>2</sub> nanocomposites dropped around 65% upon dispersing them in water. As the effect of the silica coating on the UCL intensity of UCNP is very low or undetectable in most cases,<sup>56</sup> the obvious decrease of UCL intensity from (b) to (c) is mainly attributed to the H<sub>2</sub>O solvent effect. H<sub>2</sub>O molecules can be regarded as a surface oscillator, due to their high energy vibration modes (~3600 cm<sup>-1</sup>).<sup>53,57,58</sup> The interaction between the oscillator and the doped lanthanide ions can produce an increased nonradiative relaxation of excited states and thus results in the quenching of the UCL intensity. The 30 layers of inner NaYF<sub>4</sub> shell have a modest effect on this quenching phenomenon. Although the inevitable decrease of UCL intensity was found when transferring the hydrophobic UCNP from cyclohexane to aqueous solution, the PEGylated UCNP@TEMPO@SiO<sub>2</sub> nanocomposites still maintain a strong UCL emission in aqueous solution (as shown in Fig. 7). These results indicate that the PEGylated UCNP@TEMPO@SiO<sub>2</sub> nanocomposites show promising potential for NIR excited bioimaging applications.

### 3.4 In vitro cytotoxicity test and cellular uptake of PEGylated UCNP@TEMPO@SiO<sub>2</sub> nanocomposites

The cytotoxicity of the PEGylated UCNP@TEMPO@SiO<sub>2</sub> nanocomposites was tested in HeLa cells based on an MTT assay. The cell viability is not significantly affected by the nanocomposites up to a concentration of 400 μg mL<sup>-1</sup> (Fig. 8). These data show satisfactory results that the PEGylated UCNP@TEMPO@SiO<sub>2</sub> nanocomposites can serve as promising nanoprobes with low cytotoxicity for UCL/MR dual-modality imaging. The cellular uptake efficiency of PEGylated UCNP@TEMPO@SiO<sub>2</sub>



**Fig. 8** *In vitro* cell viability of HeLa cells incubated with PEGylated UCNP@TEMPO@SiO<sub>2</sub> nanocomposites at different concentrations (0, 6.25, 12.5, 25, 50, 100, 200 and 400  $\mu\text{g mL}^{-1}$ ) for 6 h and 24 h at 37 °C.

nanocomposites were investigated by using flow cytometry and an inverted fluorescence imaging microscope. Firstly, FITC was covalently bound to the surface of PEGylated UCNP@TEMPO@SiO<sub>2</sub> nanocomposites, then the degree of cellular uptake of the nanocomposites was quantified with flow cytometry by determining the green fluorescence signal of FITC. As revealed by Fig. 9, PEGylated UCNP@TEMPO@SiO<sub>2</sub>-FITC nanocomposites were taken up by HeLa cells relative to the controlled cells, and the cellular uptake of samples increases gradually with the increasing concentration of PEGylated UCNP@TEMPO@SiO<sub>2</sub>-FITC nanocomposites (0, 8, 15, 30, 60, 125  $\mu\text{g mL}^{-1}$ ).

Besides this, in order to further verify that PEGylated UCNP@TEMPO@SiO<sub>2</sub> nanocomposites can be internalized by the cells, UCL imaging was done by utilizing a modified inverted fluorescence microscope equipped with infrared laser excitation at 980 nm. After PEGylated UCNP@TEMPO@SiO<sub>2</sub> nanocomposites (200  $\mu\text{g mL}^{-1}$ ) were incubated with HeLa cells at 37 °C for 6 h, a strong upconversion luminescence signal can be observed from the HeLa cells without any cell auto-fluorescence (Fig. 10). Meanwhile, an increasing amount of PEGylated UCNP@TEMPO@SiO<sub>2</sub> nanocomposites were internalized into the cells as the initial concentration of the samples increased (Fig. S16†). These results indicate that PEGylated UCNP@TEMPO@SiO<sub>2</sub> nanocomposites can be used as an excellent luminescence probe for cellular labeling and cell imaging.

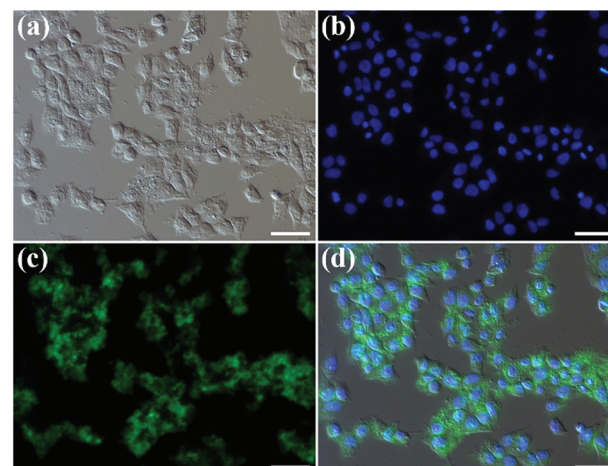


**Fig. 10** Inverted fluorescence microscope images of HeLa cells incubated with PEGylated UCNP@TEMPO@SiO<sub>2</sub> nanocomposites at 200  $\mu\text{g mL}^{-1}$  for 6 h at 37 °C. (a) Bright-field image, (b) nuclei of cells (dyed in blue with Hoechst 33258 for visualization), (c) upconversion luminescence (UCL) image collected in the green channel (500 nm to 600 nm), (d) overlay image of the three. All scale bars are 50  $\mu\text{m}$ . All images were taken under identical conditions and the nuclei were stained with Hoechst 33258.

rescence (Fig. 10). Meanwhile, an increasing amount of PEGylated UCNP@TEMPO@SiO<sub>2</sub> nanocomposites were internalized into the cells as the initial concentration of the samples increased (Fig. S16†). These results indicate that PEGylated UCNP@TEMPO@SiO<sub>2</sub> nanocomposites can be used as an excellent luminescence probe for cellular labeling and cell imaging.

### 3.5 MR relaxivity properties *in vitro* and MRI *in vivo*

The coating of TEMPO@SiO<sub>2</sub> to NaYF<sub>4</sub>:Yb,Er/NaYF<sub>4</sub> nanoparticles not only makes the UCNPs dispersible in aqueous solution and easy to functionalize with various biomolecules, but also serves to make the nanocomposites a contrast agent for T<sub>1</sub>-weighted MR imaging due to the stable paramagnetic signal from the TEMPO radicals. In order to evaluate the feasibility of PEGylated UCNPs@TEMPO@SiO<sub>2</sub> nanocomposites as an MRI contrast agent, the *r*<sub>1</sub> relaxivity and corresponding T<sub>1</sub>-weighted MR images of the PEGylated UCNP@TEMPO@SiO<sub>2</sub> nanocomposites in water were measured on a 9.4 T MRI scanner.

As shown in Fig. 11, PEGylated UCNP@TEMPO@SiO<sub>2</sub> nanocomposites exhibited an enhanced signal intensity with a dose-dependent effect. The images become brighter with increased concentrations of PEGylated UCNPs@TEMPO@SiO<sub>2</sub> nanocomposites in aqueous solution. The longitudinal relaxivity value (*r*<sub>1</sub>) of PEGylated UCNPs@TEMPO@SiO<sub>2</sub> nanocomposites was estimated to be 1.61  $\text{s}^{-1} \text{mM}^{-1}$ . The concentration of TEMPO radicals was determined by measuring the absorption of TEMPO radicals at 436 nm with a molar absorptivity coefficient of 13.3  $\text{dm}^3 \text{mol}^{-1} \text{cm}^{-1}$  (Fig. S17†). Details of the theoretical calculation are given in the ESI.† It is interesting to note that this relaxivity observed for PEGylated UCNPs@TEMPO@

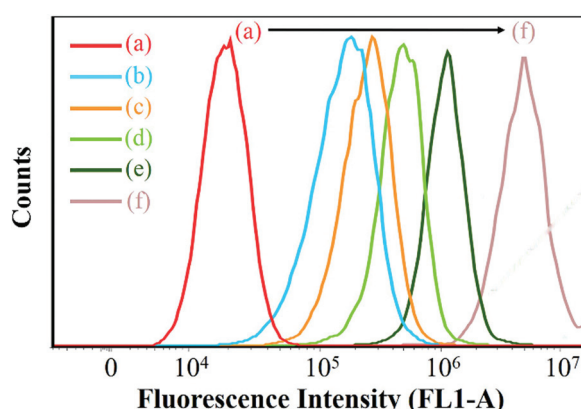


**Fig. 9** Flow cytometry analysis of HeLa cells incubated with PEGylated UCNP@TEMPO@SiO<sub>2</sub>-FITC nanocomposites at different concentrations. (a) 0  $\mu\text{g mL}^{-1}$ , as a control, (b) 8  $\mu\text{g mL}^{-1}$ , (c) 15  $\mu\text{g mL}^{-1}$ , (d) 30  $\mu\text{g mL}^{-1}$ , (e) 60  $\mu\text{g mL}^{-1}$ , (f) 125  $\mu\text{g mL}^{-1}$ . The incubation time was 6 h.

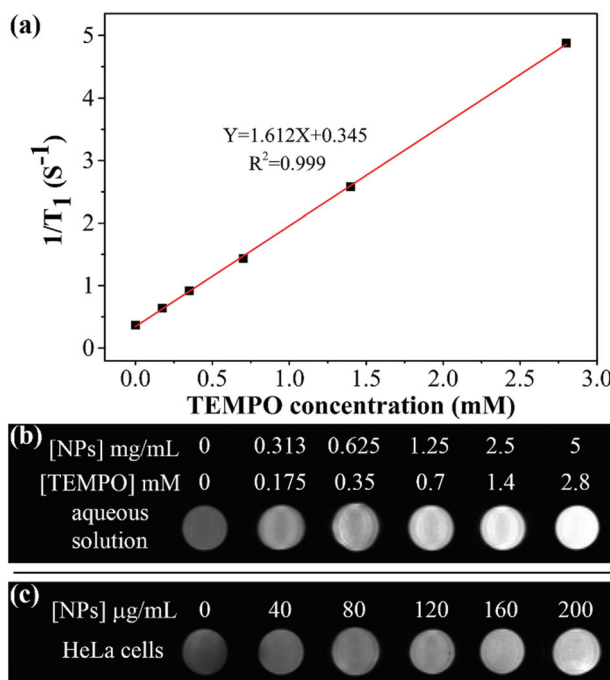


**Fig. 11** (a)  $T_1$ -weighted relaxation rates ( $1/T_1$ ,  $s^{-1}$ ) and (b)  $T_1$ -weighted MR images of PEGylated UCNPs@TEMPO@SiO<sub>2</sub> nanocomposites (NPs) as a function of [TEMPO radical] concentration (mM) in aqueous solution (9.4 T, 25 °C). (c)  $T_1$ -weighted MR images of the HeLa cells treated with PEGylated UCNPs@TEMPO@SiO<sub>2</sub> nanocomposites at different concentrations (0, 40, 80, 120, 160 and 200  $\mu\text{g mL}^{-1}$ ) for 6 h at 37 °C.

SiO<sub>2</sub> nanocomposites is about 10 times stronger than that for free TEMPO radicals (about 0.15  $s^{-1}$  mM<sup>-1</sup>) and it is impressive when compared with other nitroxide radical-based systems.<sup>41,44,59</sup> The great enhancement of  $r_1$  relaxivity is most probably attributed to the reduced tumbling rate of TEMPO radicals, thereby increasing the rotational correlation time of TEMPO.<sup>60,61</sup> Moreover, it has been reported previously that the  $r_1$  relaxivity of TEMPO radicals was proportionally increased depending on the number of paramagnetic centers in a molecule.<sup>59,62</sup> Similarly, coupling of nitroxyl molecules in a paramagnetic silica network could also significantly enhance the  $T_1$ -weighted contrast performance of nitroxide radicals. In addition, if being calculated on a per millimolar particle basis, the nanocomposites can reach a remarkably high longitudinal relaxivity ( $r_1$ ) since at least  $10^4$  nitroxide radicals have been doped within the compact network structure of SiO<sub>2</sub> shell of a single nanocomposite (the detailed calculation formulae are presented in the ESI†). These results suggest that the PEGylated UCNPs@TEMPO@SiO<sub>2</sub> nanocomposites have the potential to serve as an efficient MRI contrast agent due to their large payloads of paramagnetic centers.

To validate the diagnostic potential of the PEGylated UCNPs@TEMPO@SiO<sub>2</sub> nanocomposites used as an MRI probe at the cell level, the MR signal intensity of HeLa cells was measured after incubation with PEGylated UCNPs@TEMPO@SiO<sub>2</sub> nanocomposites at different concentrations of 40, 80, 120, 160 and 200  $\mu\text{g mL}^{-1}$  for 6 h at 37 °C. The  $T_1$ -weighted

MR contrast of HeLa cells treated with PEGylated UCNPs@TEMPO@SiO<sub>2</sub> nanocomposites was clearly enhanced when compared with that of the control cells (Fig. 11c). These results indicate that the encapsulation of TEMPO radicals within the compact network structure of SiO<sub>2</sub> may be an efficient way to make a useful contrast agent for  $T_1$ -weighted MR imaging.

To further demonstrate the performance of PEGylated UCNPs@TEMPO@SiO<sub>2</sub> nanocomposites as a nanoprobe for *in vivo* MRI, the nanocomposites were intravenously injected into nude mice for MR imaging using a 9.4 T MR imaging system. Anatomical images were acquired in the coronal and transversal planes. Comparison of pre- and post-contrast  $T_1$ -weighted coronal MR images of the whole-body showed significant contrast enhancement in several organs, with the greatest enhancement in the liver of mice (Fig. 12a and b). For transversal cross-sectional images (Fig. 12c and d), the significant contrast enhancement observed in the liver area further confirms the accumulation of these nanocomposites in the liver. Because the liver is the main organ for eliminating foreign particles, rapid accumulation in the liver and relatively slow excretion are classical behaviors of nanocomposites *in vivo*.<sup>63</sup> These observations indicate that the present PEGylated UCNPs@TEMPO@SiO<sub>2</sub> nanocomposites could circulate in the blood vessels without aggregation and were gradually cleared from reticuloendothelial systems such as the liver.<sup>14</sup> The evidence from these *in vivo* results indicate that PEGylated UCNPs@TEMPO@SiO<sub>2</sub> nanocomposites could serve as a  $T_1$ -weighted MRI contrast agent in small-animal imaging. Compared with the IONP-UCNP nanocomposites and Gd-based UCNPs, the developed PEGylated UCNPs@TEMPO@SiO<sub>2</sub> nanocomposites not only show a satisfactory MRI contrast ability but also maintain intense UCL emission. These unique pro-

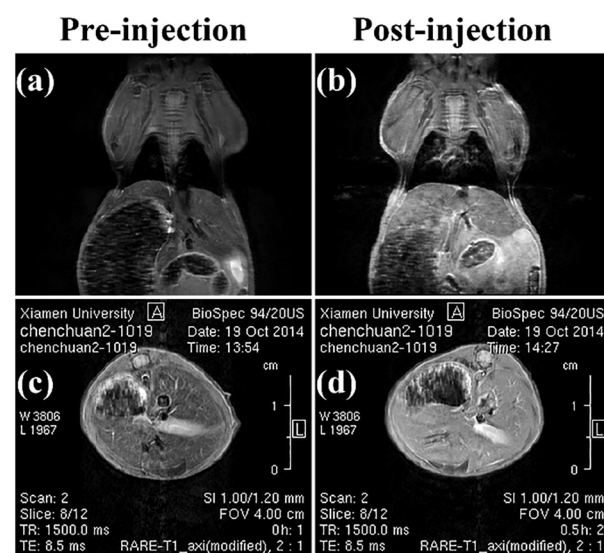


**Fig. 12** *In vivo*  $T_1$ -weighted coronal MR images of the whole body (a, b) and transversal cross-sectional images of the liver (c, d) of mice at pre-injection and at 30 min post-injection of PEGylated UCNPs@TEMPO@SiO<sub>2</sub> nanocomposites.

properties will serve them as potential multifunctional nanoprobes for UCL/MR dual-modality imaging.

## 4 Conclusions

In summary, a novel class of PEGylated UCNP@TEMPO@SiO<sub>2</sub> multifunctional nanoprobes has been developed for UCL/MR dual-modality imaging. The presence of NaYF<sub>4</sub>:Yb,Er/NaYF<sub>4</sub> UCNPs gives rise to an intense upconversion emission for UCL imaging. The compact SiO<sub>2</sub> shell can protect the embedded TEMPO radicals from being reduced to the corresponding hydroxylamines in biological environments when compared with free radicals. The TEMPO@SiO<sub>2</sub> shell can provide the paramagnetic property and induce the enhancement of the positive-contrast of MR imaging. The cytotoxicity assay shows PEGylated UCNP@TEMPO@SiO<sub>2</sub> nanocomposites possess low toxicity. *In vitro* UCL imaging study confirms the PEGylated UCNP@TEMPO@SiO<sub>2</sub> nanocomposites are well suited for cell imaging. The preliminary *in vivo* MRI results indicate PEGylated UCNP@TEMPO@SiO<sub>2</sub> nanocomposites can serve as T<sub>1</sub>-weighted MRI contrast agents. Therefore, we expect that such multifunctional nanoprobes, combining the advantages of a TEMPO-based paramagnetic MRI contrast agent and the upconversion luminescence of core-shell NaYF<sub>4</sub>:Yb,Er/NaYF<sub>4</sub> UCNPs, will find extensive applications in UCL/MR dual-modality bioimaging.

## Acknowledgements

This work was financially supported by the National Basic Research Program of China (973 Program) (2011CB910403, 2013CB933703,) and the National Nature Science Foundation of China (NSFC grants 31371012 and 81171448).

## Notes and references

- 1 J. Kim, Y. Piao and T. Hyeon, *Chem. Soc. Rev.*, 2009, **38**, 372–390.
- 2 A. Louie, *Chem. Rev.*, 2010, **110**, 3146–3195.
- 3 J. Yao, M. Yang and Y. X. Duan, *Chem. Rev.*, 2014, **114**, 6130–6178.
- 4 Y. I. Park, K. T. Lee, Y. D. Suh and T. Hyeon, *Chem. Soc. Rev.*, 2014, DOI: 10.1039/C4CS00173G.
- 5 L. N. Sun, Z. W. Wei, H. G. Chen, J. L. Liu, J. J. Guo, M. Cao, T. Q. Wen and L. Y. Shi, *Nanoscale*, 2014, **6**, 8878–8883.
- 6 L. N. Sun, T. Liu, Y. N. Qiu, J. L. Liu, L. Y. Shi and O. S. Wolfbeis, *Microchim. Acta*, 2014, **181**, 775–781.
- 7 L. Cheng, C. Wang and Z. Liu, *Nanoscale*, 2013, **5**, 23–37.
- 8 Z. W. Wei, L. N. Sun, J. L. Liu, J. Zhang, H. R. Yang, Y. Yang and L. Y. Shi, *Biomaterials*, 2014, **35**, 387–392.
- 9 S. L. Gai, C. X. Li, P. P. Yang and J. Lin, *Chem. Rev.*, 2014, **114**, 2343–2389.
- 10 L. Cheng, K. Yang, Y. G. Li, J. H. Chen, C. Wang, M. W. Shao, S. T. Lee and Z. Liu, *Angew. Chem., Int. Ed.*, 2011, **50**, 7385–7390.
- 11 W. Feng, C. M. Han and F. Y. Li, *Adv. Mater.*, 2013, **25**, 5287–5303.
- 12 Y. Sun, X. J. Zhu, J. J. Peng and F. Y. Li, *ACS Nano*, 2013, **7**, 11290–11300.
- 13 R. Kumar, M. Nyk, T. Y. Ohulchanskyy, C. A. Flask and P. N. Prasad, *Adv. Funct. Mater.*, 2009, **19**, 853–859.
- 14 J. Zhou, M. X. Yu, Y. Sun, X. Z. Zhang, X. J. Zhu, Z. H. Wu, D. M. Wu and F. Y. Li, *Biomaterials*, 2011, **32**, 1148–1156.
- 15 Q. F. Xiao, X. P. Zheng, W. B. Bu, W. Q. Ge, S. J. Zhang, F. Chen, H. Y. Xing, Q. G. Ren, W. P. Fan, K. L. Zhao, Y. Q. Hua and J. L. Shi, *J. Am. Chem. Soc.*, 2013, **135**, 13041–13048.
- 16 D. L. Ni, W. B. Bu, S. J. Zhang, X. P. Zheng, M. Li, H. Y. Xing, Q. F. Xiao, Y. Y. Liu, Y. Q. Hua, L. P. Zhou, W. J. Peng, K. L. Zhao and J. L. Shi, *Adv. Funct. Mater.*, 2014, **24**, 6613–6620.
- 17 D. L. Ni, J. W. Zhang, W. B. Bu, H. Y. Xing, F. Han, Q. F. Xiao, Z. W. Yao, F. Chen, Q. J. He, J. N. Liu, S. J. Zhang, W. P. Fan, L. P. Zhou, W. J. Peng and J. L. Shi, *ACS Nano*, 2014, **8**, 1231–1242.
- 18 L. N. Sun, X. Q. Ge, J. L. Liu, Y. N. Qiu, Z. W. Wei, B. Tian and L. Y. Shi, *Nanoscale*, 2014, **6**, 13242–13252.
- 19 Y. Zhang, G. K. Das, V. Vijayaragavan, Q. C. Xu, P. Padmanabhan, K. K. Bhakoo, S. T. Selvan and T. T. Y. Tan, *Nanoscale*, 2014, **6**, 12609–12617.
- 20 B. Liu, C. X. Li, P. A. Ma, Y. Y. Chen, Y. X. Zhang, Z. Y. Hou, S. S. Huang and J. Lin, *Nanoscale*, 2015, **7**, 1839–1848.
- 21 D. Wang, L. Ren, X. Zhou, X. Z. Wang, J. Zhou, Y. Han and N. Kang, *Nanotechnology*, 2012, **23**, 225705.
- 22 Y. Wang, L. Ji, B. B. Zhang, P. H. Yin, Y. Y. Qiu, D. Q. Song, J. Y. Zhou and Q. Li, *Nanotechnology*, 2013, **24**, 175101.
- 23 F. Chen, W. B. Bu, S. J. Zhang, X. H. Liu, J. N. Liu, H. Y. Xing, Q. F. Xiao, L. P. Zhou, W. J. Peng, L. Z. Wang and J. L. Shi, *Adv. Funct. Mater.*, 2011, **21**, 4285–4294.
- 24 Z. Q. Li and Y. Zhang, *Nanoscale*, 2010, **2**, 1240–1243.
- 25 A. Xia, M. Chen, Y. Gao, D. M. Wu, W. Feng and F. Y. Li, *Biomaterials*, 2012, **33**, 5394–5405.
- 26 S. L. Gai, P. P. Yang, C. X. Li, W. X. Wang, Y. L. Dai, N. Niu and J. Lin, *Adv. Funct. Mater.*, 2010, **20**, 1166–1172.
- 27 L. Cheng, K. Yang, Y. G. Li, X. Zeng, M. W. Shao, S. T. Lee and Z. Liu, *Biomaterials*, 2012, **33**, 2215–2222.
- 28 J. Berliner and H. Fujii, *Science*, 1985, **227**, 517–519.
- 29 Z. Zhelev, R. Bakalova, I. Aoki, K. Matsumoto, V. Gadjeva, K. Anzai and I. Kanno, *Mol. Pharmaceutics*, 2009, **6**, 504–512.
- 30 J. H. Ortony, C. J. Newcomb, J. B. Matson, L. C. Palmer, P. E. Doan, B. M. Hoffman and S. I. Stupp, *Nat. Mater.*, 2014, **13**, 812–816.
- 31 A. Hahn, S. Reschke, S. Leimkuehler and T. Risse, *J. Phys. Chem. B*, 2014, **118**, 7077–7084.
- 32 L. B. Du, S. P. Huang, Q. F. Zhuang, H. Y. Jia, A. Rockenbauer, Y. P. Liu, K. J. Liu and Y. Liu, *Nanoscale*, 2014, **6**, 1646–1652.

- 33 K. Matsumoto, F. Hyodo, A. Matsumoto, A. P. Koretsky, A. L. Sowers, J. B. Mitchell and M. C. Krishna, *Clin. Cancer Res.*, 2006, **12**, 2455–2462.
- 34 F. Hyodo, K. Chuang, A. G. Goloshevsky, A. Sulima, G. L. Griffiths, J. B. Mitchell, A. P. Koretsky and M. C. Krishna, *J. Cereb. Blood Flow Metab.*, 2008, **28**, 1165–1174.
- 35 B. P. Soule, F. Hyodo, K. Matsumoto, N. L. Simone, J. A. Cook, M. C. Krishna and J. B. Mitchell, *Free Radical Biol. Med.*, 2007, **42**, 1632–1650.
- 36 K. Takechi, H. Tamura, K. Yamaoka and H. Sakurat, *Free Radical Res.*, 1997, **26**, 483–496.
- 37 T. Yoshitomi, D. Miyamoto and Y. Nagasaki, *Biomacromolecules*, 2009, **10**, 596–601.
- 38 T. Yoshitomi, R. Suzuki, T. Mamiya, H. Matsui, A. Hirayama and Y. Nagasaki, *Bioconjugate Chem.*, 2009, **20**, 1792–1798.
- 39 X. L. Zhuang, C. S. Xiao, K. Oyaizu, N. Chikushi, X. S. Chen and H. Nishide, *J. Polym. Sci., Part A: Polym. Chem.*, 2010, **48**, 5404–5410.
- 40 M. Gussoni, F. Greco, P. Ferruti, E. Ranucci, A. Ponti and L. Zetta, *New J. Chem.*, 2008, **32**, 323–332.
- 41 C. S. Winalski, S. Shortkroff, E. Schneider, H. Yoshioka, R. V. Mulkern and G. M. Rosen, *Osteoarthritis Cartilage*, 2008, **16**, 815–822.
- 42 M. C. Emoto, K. Yamada, M. Yamato and H. G. Fujii, *Neurosci. Lett.*, 2013, **546**, 11–15.
- 43 E. Tanimoto, S. Karasawa, S. Ueki, N. Nitta, I. Aoki and N. Koga, *RSC Adv.*, 2013, **3**, 3531–3534.
- 44 E. J. Rivera, R. Sethi, F. Qu, R. Krishnamurthy, R. Muthupillai, M. Alford, M. A. Swanson, S. S. Eaton, G. R. Eaton and L. J. Wilson, *Adv. Funct. Mater.*, 2012, **22**, 3691–3698.
- 45 H. C. Chan, K. Sun, R. L. Magin and H. M. Swartz, *Bioconjugate Chem.*, 1990, **1**, 32–36.
- 46 V. Muhr, Th. Hirsch, S. Wilhelm and O. S. Wolfbeis, *Acc. Chem. Res.*, 2014, **47**, 3481–3493.
- 47 C. Ghica and P. Ionita, *J. Mater. Sci.*, 2007, **42**, 10058–10064.
- 48 R. Ciriminna, J. Blum, D. Avnir and M. Pagliaro, *Chem. Commun.*, 2000, 1441.
- 49 C. Tansakul, E. Lilie, E. D. Walter, F. Rivera III, A. Wolcott, J. Z. Zhang, G. L. Millhauser and R. Braslau, *J. Phys. Chem. C*, 2010, **114**, 7793–7805.
- 50 E. Yoshida and T. Tanaka, *Colloid Polym. Sci.*, 2006, **285**, 135–144.
- 51 J. Fuchs, N. Groth, T. Herrling and G. Zimmer, *Free Radical Biol. Med.*, 1997, **22**, 967–976.
- 52 H. Dong, L. D. Sun and C. H. Yan, *Nanoscale*, 2013, **5**, 5703–5714.
- 53 G. Y. Chen, H. Ågren, T. Y. Ohulchanskyy and P. N. Prasad, *Chem. Soc. Rev.*, 2015, DOI: 10.1039/C4CS00170B.
- 54 X. M. Li, D. K. Shen, J. P. Yang, C. Yao, R. C. Che, F. Zhang and D. Y. Zhao, *Chem. Mater.*, 2013, **25**, 106–112.
- 55 P. Huang, W. Zheng, S. Y. Zhou, D. T. Tu, Z. Chen, H. M. Zhu, R. F. Li, E. Ma, M. D. Huang and X. Y. Chen, *Angew. Chem., Int. Ed.*, 2014, **53**, 1252–1257.
- 56 A. Sedlmeier and H. H. Gorris, *Chem. Soc. Rev.*, 2015, DOI: 10.1039/C4CS00186A.
- 57 J. C. Boyer, M. P. Manseau, J. I. Murray and F. C. J. M. van Veggel, *Langmuir*, 2010, **26**, 1157–1164.
- 58 F. Wang, J. Wang and X. G. Liu, *Angew. Chem., Int. Ed.*, 2010, **49**, 7456–7460.
- 59 K. Matsumoto, H. Yakumaru, M. Narazaki, H. Nakagawa, K. Anzai, H. Ikehira and N. Ikota, *Magn. Reson. Imaging*, 2008, **26**, 117–121.
- 60 J. Rudovský, M. Botta, P. Hermann, K. I. Hardcastle, I. Lukeš and S. Aime, *Bioconjugate Chem.*, 2006, **17**, 975–987.
- 61 S. Aime, M. Botta, M. Fasano, S. G. Crich and E. Terreno, *JBIC, J. Biol. Inorg. Chem.*, 1996, **1**, 312–319.
- 62 C. S. Winalski, S. Shortkroff, R. V. Mulkern, E. Schneider and G. M. Rosen, *Magn. Reson. Med.*, 2002, **48**, 965–972.
- 63 L. Q. Xiong, T. S. Yang, Y. Yang, C. J. Xu and F. Y. Li, *Biomaterials*, 2010, **31**, 7078–7085.